



Weighing Uranus' Moon Cressida with the η Ring

Robert O. Chancia¹, Matthew M. Hedman¹, and Richard G. French²

¹ Department of Physics, University of Idaho, Moscow, ID 83844-0903, USA; rchancia@uidaho.edu

² Astronomy Department, Wellesley College, Wellesley, MA 02481, USA

Received 2017 June 19; revised 2017 August 9; accepted 2017 August 21; published 2017 September 20

Abstract

The η ring is one of the narrow rings of Uranus, consisting of a dense core that is 1–2 km wide and a diffuse outer sheet spanning about 40 km. Its dense core lies just exterior to the 3:2 Inner Lindblad Resonance of the small moon Cressida. We fit the η ring radius residuals and longitudes from a complete set of both ground-based and *Voyager* stellar and radio occultations of the Uranian rings spanning 1977–2002. We find variations in the radial position of the η ring that are likely generated by this resonance, and take the form of a 3-lobed structure rotating at an angular rate equal to the mean motion of the moon Cressida. The amplitude of these radial oscillations is 0.667 ± 0.113 km, which is consistent with the expected shape due to the perturbations from Cressida. The magnitude of these variations provides the first measurement of the mass and density of the moon Cressida ($m = (2.5 \pm 0.4) \times 10^{17}$ kg and $\rho = 0.86 \pm 0.16$ g cm⁻³) or, indeed, any of Uranus' small inner moons. A better grasp of inner Uranian satellite masses will provide another clue to the composition, dynamical stability, and history of Uranus' tightly packed system of small moons.

Key words: planets and satellites: individual (Uranus, Cressida) – planets and satellites: rings

1. Introduction

In 1977 March, Elliot et al. (1977), Millis et al. (1977), and Bhattacharyya & Kuppaswamy (1977) discovered nine narrow rings around the planet Uranus by measuring the light blocked by each ring before and after Uranus occulted the star SAO158687. Since then, the Uranian rings have been studied extensively with ground-based stellar occultations (Millis & Wasserman 1978; Nicholson et al. 1978, 1981; Elliot et al. 1981a, 1981b, 1983, 1984, 1987; French et al. 1982, 1986a, 1986b, 1988, 1996; Sicardy et al. 1982). Occultations provide very precise radial locations of the rings at different longitudes in their orbits around Uranus. French et al. (1988) found that the main rings of Uranus consist of six measurably eccentric rings (6, 5, 4, α , β , and ϵ) and three nearly circular rings (η , γ , and δ). In the past, measurements of the η ring's radius have not shown the ring to be anything but circular. The η ring also features a broad low optical depth sheet extending approximately 40 km exterior to its narrow core (Elliot et al. 1983).

During the *Voyager 2* flyby of Uranus, Smith et al. (1986) discovered 10 new small inner moons, but no one has ever measured their masses or densities. Nine of the moons orbit within a radial range of 20,000 km, making the group one of the most tightly packed systems of interacting satellites in our solar system. Lissauer (1995) estimated the masses of the inner moons assuming densities equal to that of the larger moon Miranda (Jacobson et al. 1992) and shapes estimated with photometry (Thomas et al. 1989), but stated that at least some of Uranus' small inner moons are significantly less massive than these estimates. The lifetime of this system is highly sensitive to the masses of the individual satellites (French et al. 2015). In fact, prior to the knowledge of the even less stable moon Cupid (Showalter & Lissauer 2003; French & Showalter 2012), Duncan & Lissauer (1997) showed that Desdemona could collide with either Cressida or Juliet within the next 4–100 million years, depending on the masses of the satellites involved. The discovery of the dusty ν and μ rings (Showalter & Lissauer 2006), near the orbits of

Portia/Rosalind and Mab, respectively, hints at the possibility of an evolving inner ring–moon system dominated by accretion (Tiscareno et al. 2013). Kumar et al. (2015) also argue that anomalies in Mab's orbital motion may be explained by a ring–moon system that is undergoing re-accretion after a recent catastrophic disruption.

Here, we investigate a complete set of Uranian η ring occultation observations spanning their discovery in 1977 through 2002. We find that the η ring's radii exhibit a three-lobed structure rotating around Uranus at the mean motion of the moon Cressida. We argue that this structure is a result of the η ring's close proximity to Cressida's 3:2 inner Lindblad resonance (ILR). One of the maxima in the ring's radius aligns with Cressida, as expected for the stable ring structure located exterior to the resonant radius. The measured radial amplitude of this ring structure and its distance from the resonance allow us to estimate Cressida's mass and thus obtain the first gravity-based mass measurement of any inner Uranian moon.

We have only been able to find three previous mentions of the Cressida 3:2 ILR and its association with the η ring. Porco & Goldreich (1987) identified the most relevant resonances in the Uranian ring–moon system and made a case for Cordelia and Ophelia shepherding the outermost ϵ ring through torques generated by the Lindblad resonances located appropriately on the ring's inner and outer edges (Goldreich & Porco 1987). They also note single resonances that could be perturbing the γ and δ rings. Finally, they state, “The only isolated first-order satellite resonances which fall near any of the remaining rings are located interior to the η ring.” Porco & Goldreich (1987, p. 728) list both the Cressida 3:2 and the Cordelia 13:12 resonances, located at $a = 47171.6 \pm 0.3$ km and $a = 47173.0 \pm 0.3$ km, respectively. These resonances fall 3–5 km radially interior to the η ring. They calculate the widths of both resonances to be ~ 1 km and dismiss the possibility that either resonances is perturbing the η ring. Murray & Thompson (1988) later marked the location of the Cressida 3:2 ILR in their figure, displaying a radial scan of a high phase image of the Uranian rings acquired by *Voyager 2*. Subsequently, Murray & Thompson (1990) noted that this

resonance needs to be re-examined using updated satellite parameters. At the time, with a smaller data set, there was no detection of either an $m = 3$ or an $m = 13$ mode in the η ring, nor any other modes due to resonances with known satellites having observed effects on any of the other previously noted rings' edges (French et al. 1988). Thus, it was only sensible to dismiss these resonances, and it is reasonable that they have not been of interest since. We are only able to make this discovery now because we have a larger set of occultation data extending from 1977 through 2002.

We present the data used in this analysis in Section 2 and describe our ring particle streamline model and our mode detection methods in Section 3. In Section 4, we report the parameters of our fit to the η ring and calculate the mass and density of Cressida. Finally, in Section 5, we discuss potential implications for the dynamical stability of the tightly packed system of inner Uranian moons and the possible composition of Cressida.

2. Observational Data

The observational data used for this analysis consist of 49 individual occultation observations of the η ring. In the Appendix, we have tabulated each occultation's ring intercept time, inertial longitude, and mid-radius determined using a simple square-well model for profile fitting, developed by Elliot et al. (1984) and used in later orbit determinations of the Uranian rings (French et al. 1986a, 1986b, 1988, 1991). Of these 49 observations, 46 are Earth-based stellar occultations, 2 are *Voyager 2* Radio Science Subsystem (RSS) radio occultations, and 1 is a *Voyager 2* Photopolarimeter Subsystem (PPS) stellar occultation. Several of the observations are ingress and egress pairs from the same occultation of Uranus and its rings.

For each Earth-based occultation, an instrument recorded the brightness of the background star as a function of time. As the Earth moves relative to Uranus, the rings can block the star's light, leaving each ring's mark as a sharp decrease in the recorded brightness of the star for some amount of time related to the width of the ring. Typically, the observations were detected with an InSb photometer in the $2.2 \mu\text{m}$ band, using the K filter, where Uranus is fainter than the rings. Most observations provided limited information about the radial structure within the rings, and here we are making use only of the estimate of the radius of the mid-point of each ring occultation profile. Interested readers should see Elliot (1979) for a review of stellar occultation studies of the solar system and Elliot & Nicholson (1984) for a review of this observation method specific to the rings of Uranus.

To identify possible Uranus occultation opportunities, Taylor (1973) compared positions of Uranus to stellar positions in the Smithsonian Astrophysical Observatory (SAO) catalog. Once the rings were discovered, it became more appropriate to utilize dimmer stars that are bright in the $2.2 \mu\text{m}$ band. Thus, Klemola & Marsden (1977) searched for stars on photographic plates containing star fields ahead of Uranus and created a list of ideal future occultation observations. Additional lists of this type were compiled by Klemola et al. (1981), Mink & Klemola (1982, 1985), Nicholson et al. (1988), and Klemola & Mink (1991).

The *Voyager 2* PPS stellar occultation only detected the η ring on egress (Lane et al. 1986; Colwell et al. 1990). In the case of the *Voyager 2* RSS occultations, the RSS instrument illuminated the rings at 3.6 and 13 cm wavelengths in the

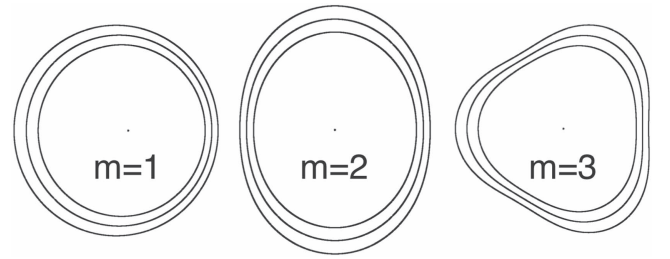


Figure 1. The above shapes are an exaggerated representation of the m -lobed ring streamlines we detect in the Uranian rings. For each case of m , we have shown three streamlines with slightly different semimajor axes and a positive eccentricity gradient. Our addition of an eccentricity gradient results in a narrower ring width at periapsis, as is the case for several of the Uranian rings.

direction of Earth once beyond the ring plane. Stations on Earth detected the diffracted signal and relative phase change, to later be reconstructed into high-resolution radial optical depth profiles after the removal of diffraction effects (Tyler et al. 1986; Gresh et al. 1989). Presently, ground-based occultation opportunities are rare because Uranus has passed out of the dense Milky Way background, drastically reducing the density of appropriate background stars. The rings are also no longer as open to our view from Earth as they were in the 1980s because the apparent aspect of the ring plane as viewed from Earth changes over time.

3. Ring Particle Streamline Model and Fitting Method

The procedure used here follows that of French et al. (1986b, 1988, 1991) for the Uranian rings, more recently employed by Hedman et al. (2010), Nicholson et al. (2014a, 2014b), and French et al. (2016b) for analyses of Saturn's non-circular narrow rings, gaps, and edges. After taking into account any inclination relative to the equatorial plane, the majority of narrow rings are well-fit by simple precessing Keplerian ellipses whose radii are described by:

$$r(\lambda, t) = \frac{a(1 - e^2)}{1 + e \cos f}, \quad (1)$$

where the true anomaly $f = \lambda - \varpi_0 - \dot{\varpi}(t - t_0)$. Here, the radius of the ring will vary with longitude λ and time t , where a and e are the ring's semimajor axis and eccentricity, ϖ_0 is the ring's longitude of periapsis at the time t_0 , and $\dot{\varpi}$ is the ring's apsidal precession rate. We can approximate a nearly circular ($e \simeq 0$) ring's radii as $r \simeq a(1 - e \cos f)$.

Additionally, several rings are found to contain forced radial oscillations and in a few cases there are even rings whose structures are dominated by free normal mode oscillations. In these cases, the structures are distinct from circles or ellipses and their radii are described by:

$$r(\lambda, t) \simeq a - A_m \cos(m\theta), \quad (2)$$

where $\theta = \lambda - \Omega_p(t - t_0) - \delta_m$, following the formalism of Nicholson et al. (2014a, 2014b) and French et al. (2016a). Here, the systematic radial oscillations of the rings form an m -lobed figure rotating around their planet at a pattern speed Ω_p with a radial amplitude A_m and phase δ_m . We show some exaggerated models of m -lobed ring streamlines, resulting from both free normal modes and Lindblad resonances (see Figure 1). While individual particles follow normal elliptical orbits, described by Equation (1), the ring as a whole consists of

streamlines with m azimuthally symmetric radial minima and maxima rotating around the planet with the frequency

$$\Omega_p \simeq \frac{(m-1)n + \dot{\varpi}_{\text{sec}}}{m}. \quad (3)$$

Here, the mean motion n and apsidal precession rate $\dot{\varpi}_{\text{sec}}$ are functions of the semimajor axis a of the ring, and m can be any positive or negative integer. If we consider the case of $m = 1$ we find that $\Omega_p = \dot{\varpi}_{\text{sec}}$, $A_1 = ae$, and $\delta_1 = \varpi_0$, so that r is equivalent to the approximation of Equation (1) above.

In the case of a free normal mode oscillation, the pattern speed will be equal to the expected pattern speed obtained by evaluating Equation (3) at the semimajor axis of the ring. However, if the ring is perturbed by a satellite through a first-order Lindblad resonance, then the ring structure will have a forced pattern speed matching the mean motion of the perturbing satellite $n_s = \Omega_p$ and will differ from the expected pattern speed slightly based on the ring's separation from the exact radius of the resonance $|a - a_{\text{res}}|$. The ring is perturbed by the satellite due to the near commensurate ratio of the ring particles' orbital periods and the period of the perturbing satellite. As such, first-order Lindblad resonances are defined by $|m| : |m - 1|$, where for every $|m|$ orbits of the ring particle, there are $|m - 1|$ orbits of the corresponding satellite. In the majority of cases, the perturbing satellite lies at a larger semimajor axis than the ring ($a_s > a$). The relevant resonances in this case are called ILR and are assigned positive values of m . In the rare case of a satellite located interior to the rings, it is possible to have both ILR and outer Lindblad resonances (OLR) at locations within the rings, allowing for negative values of m .

The condition for a first-order Lindblad resonance is that the resonant argument

$$\varphi = m(\lambda - \lambda_s) - (\lambda - \varpi) \quad (4)$$

is constant in time. Here, λ and λ_s refer to the longitudes of a ring particle and the satellite, respectively, and ϖ is the longitude of periapsis of the ring particle. If we consider a conjunction of the ring particle and the satellite ($\lambda - \lambda_s = 0$) occurring when the ring particle is also located at its longitude of periapsis ($\lambda - \varpi = 0$), then the condition that φ is constant implies that all future conjunctions will occur when the ring particle is near periapsis. In general, this means that the ring particle will always be in the same phase of its orbit when it passes longitudinally close to the satellite. This allows the perturbing satellite to force the eccentricity and periapsis locations of streamlines located near the resonance. In Figure 2, we show a cartoon model of the resulting streamlines surrounding a 3:2 ILR in the co-rotating frame of the perturbing satellite. Interior (exterior) to the resonant radius, marked with the dashed line, the streamlines are stable when oriented such that one of the three periapses (apoapses) is aligned with the satellite.

In short, our procedure is a search for patterns in the varying mid-radii measurements of the rings. Each ring occultation observation provides the ring's radius at a particular longitude and time. To search for patterns in each ring, we need the observed parameters, an m value to test, and the resulting expected pattern speeds for that m value. For each test of m , we compute the expected pattern speed for the semimajor axis of the ring using Equation (3) and create an array of 100,000

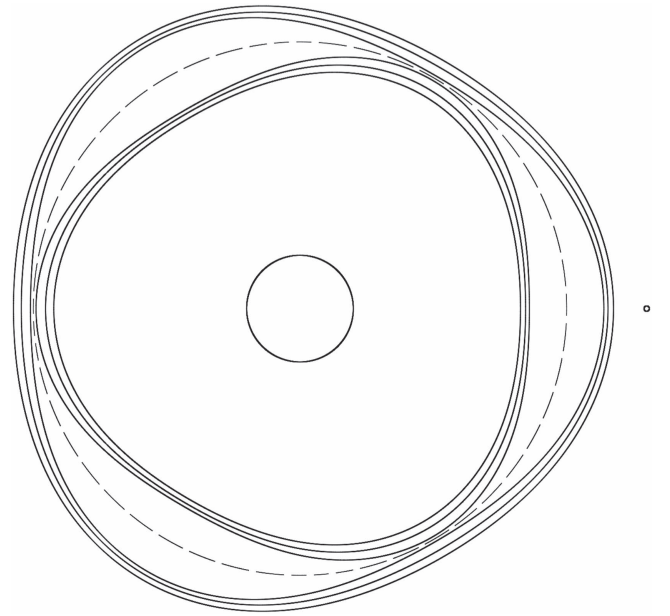


Figure 2. An exaggerated cartoon model of ring particle streamlines around a planet and near a 3:2 ILR with an exterior moon, in the co-rotating frame of the moon. We have marked the resonant radius with a dashed line and included three ring particle streamlines on either side of the resonance. This shows the stable configuration on either side of the resonance, where a periapse (apoapse) is aligned with the moon interior (exterior) to the resonance.

pattern speeds, evenly spaced in increments of $0.00001/\text{day}$, surrounding the expected pattern speed. Using each pattern speed, we calculate $m\theta$, for every ring observations' longitude λ and time t , using an initial epoch time t_0 of UTC 1977 March 10 20:00:00.00. We can then compute the observed ring radii r versus $m\theta \bmod 360^\circ$ and fit the data to a single sinusoid. The resulting fit parameters are a , A_m , and δ_m , allowing us to compute model values of r using Equation (2). We compute the rms deviation of the observed radii and the model radii for each m 's 100,000 test pattern speeds and look for an rms minimum to identify the best fitting pattern speed.

We first checked our algorithms by searching for known structures in the Uranian rings. In several rings (6, 5, 4, α , β , and ϵ), we can easily detect rms deviations that drop to nearly zero (sub-km) with the proper pattern speed and m input. These are the rings that largely follow classical Keplerian ellipses ($m = 1$) and whose pattern speeds equal the rings' apsidal precession rate, $\Omega_p = \dot{\varpi}_{\text{sec}}$. The η , γ , and δ rings are nearly circular and their residuals are relatively larger when fit with a low amplitude $m = 1$ ellipse. We are also able to identify the known $m = 2$ structure of the δ ring and the combination of $m = 0$ and $m = 1$ for the γ ring (French et al. 1986b).

We decided to identify the strongest resonances in the Uranian rings to have a better idea of the resonantly forced modes that are the most likely to be detected. To quantify the “strength” of the resonances in the system, we chose to compare the expected forced radial amplitude on rings near each of the possible resonances in the main ring system. We use Equation (10.22) from Chapter 10 of Murray & Dermott (1999),

$$A_m = \frac{2\alpha a^2(m_s/m_p)|f_d|}{3(j-1)|a - a_{\text{res}}|} \quad (5)$$

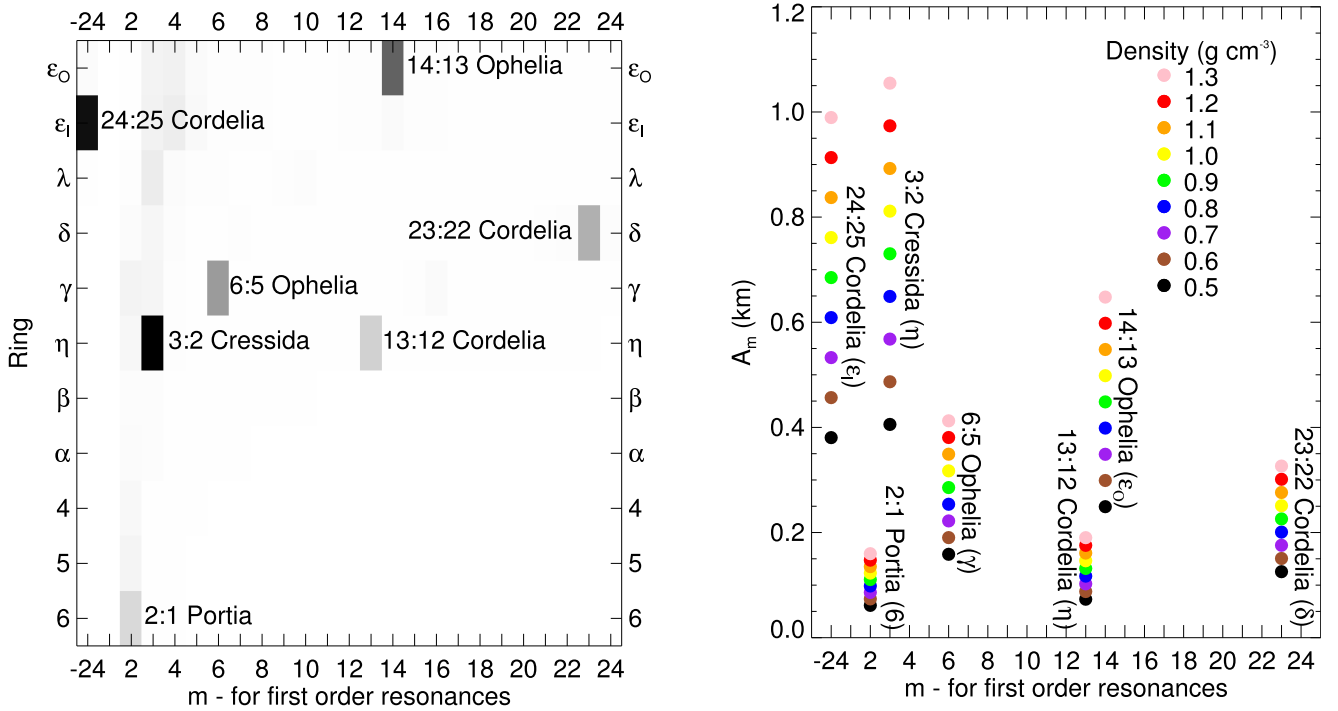


Figure 3. The left mosaic shows the relative forced amplitude (darker = larger amplitude) of all first-order resonances of inner moons out to Perdita interacting with the Uranian rings, assuming the moons each have a density of 1.3 g cm^{-3} . The largest amplitude resonances are labeled, while the fainter patches in the mosaic are evidence of resonances within the system that do not fall close enough to any rings and would have much smaller amplitudes. The actual values of the significant resonances are plotted on the right side to compare with the mosaic but with the addition of a range of moon densities ($0.5\text{--}1.3 \text{ g cm}^{-3}$), calculated using Equation (5).

where A_m is the forced radial amplitude of a ring particle in the vicinity of a Lindblad resonance (Goldreich & Tremaine 1982; Porco & Nicholson 1987). This amplitude is a function of the ratio of the perturbing satellite and central planet masses m_s/m_p , the radial separation of the ring and the resonance $|a - a_{\text{res}}|$, the ratio of the ring and satellite semimajor axes $\alpha = a/a_s$, and the Laplace factor f_d , that depends on j , the integer coefficient of the satellites longitude in the resonant argument, which is equivalent to m in the case of a first-order Lindblad resonance. As shown in Figure 10.10 of Murray & Dermott (1999), $\frac{2\alpha |f_d|}{j-1}$ varies between 1.5 and 1.6, depending on j . Note that Equation (5) is not necessarily applicable for all cases. If $|a - a_{\text{res}}|$ is smaller than the resonance half-width, then A_m calculated using Equation (5) is not a good estimation of the radial amplitude produced by the resonance because in this regime, neighboring streamlines will cross and collisional dissipation cannot be ignored.

In Figure 3, we display the expected forced amplitude on all 10 rings (inner and outer edges for the ϵ ring) due to all possible first-order Lindblad resonances of all Uranian moons out to Perdita. For the estimated mass of each moon, we use the radius measurements of Karkoschka (2001a) and Showalter & Lissauer (2006) and consider a range of densities from 0.5 to 1.3 g cm^{-3} . In the left half of Figure 3, all resonances mentioned by Porco & Goldreich (1987) are apparent in addition to a previously unexplored 2:1 ILR with Portia in the proximity of the 6 ring. In the right side of Figure 3, we compare the amplitudes of the strongest resonances over a range of moon densities. The fainter patches in the left side of Figure 3 are due to resonances inducing much weaker amplitudes due to their large distance from the rings. Despite the separation in semimajor axis of the η ring from the Cressida

3:2 ILR, the η ring is expected to be the most perturbed of all the Uranian rings in this framework. The next largest expected amplitudes are the Cordelia 24:25 OLR and the Ophelia 14:13 ILR that are thought to play a roll in shepherding the ϵ ring. If this is a realistic estimation of the strength of the resonances in the system, in the future we may be able to detect the $m = -24$ mode on the inner edge of the ϵ ring, which was previously detected by French & Nicholson (1995) with occultation data and by Showalter (2011) with images showing the ring's longitudinal brightness variations. Detecting the ϵ ring edge modes will first require determining the ring's edge positions and the removal of the larger amplitude $m = 1$ normal mode that dominates its structure. Our analysis of these ring residuals as well as those for the other rings, whose structure is dominated by previously known normal modes, is ongoing and will be presented in a subsequent publication.

4. Results

After searching mode values from $m = -25$ to $+25$ of all the rings, the strongest new feature we've found is an $m = 3$ structure of the η ring consistent with the expectations discussed above. In Figure 4, we show the shallow minimum in rms for our η ring $m = 3$ fits. The top plot shows the rms deviations of the model radii from the observed radii at each pattern speed for $m = 3$, zoomed in on the minimum. Listed are the best fitting pattern speed, the semimajor axis of the Cressida 3:2 ILR, and the expected pattern speed for an $m = 3$ normal mode marked by the dashed line. Note that the best fitting pattern speed and the expected pattern speed for the semimajor axis of the η ring are offset because this is not a normal mode oscillation, but is instead the effect of a resonance with a satellite whose perturbations force the pattern speed to match the satellite's mean motion. We further refine our best-fit

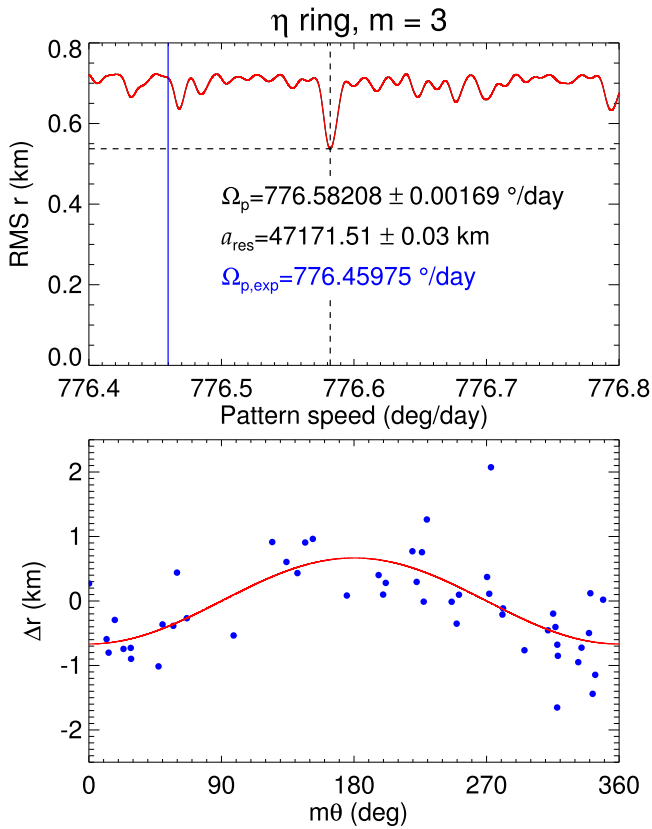


Figure 4. The upper plot shows the rms deviations of the observed radii, r , and the model fit (Equation (2)) for a range of pattern speeds, Ω_p . Listed in the top plot are the best fitting pattern speed and the corresponding radial location of the resonance, a_{res} . The blue line refers to the expected pattern speed for an $m = 3$ normal mode oscillation. The lower plot shows the best fitting model (red line) and observed radii plotted vs. $m\theta = m[\lambda - \Omega_p(t - t_0) - \delta_m]$ after subtracting the semimajor axis of the ring ($\Delta r = r - a$).

solution and formal errors by applying the best-fit parameters (a , A_m , δ_m , and Ω_p) as a set of starting parameters for MPFIT, a nonlinear least-squares fitting IDL function (Markwardt et al. 2009). We have initially assumed an uncertainty of 1 km in each of the 49 observed radii of the η ring, but found a reduced chi-squared of $0.308 \ll 1$. We fit again to obtain the listed errors using the standard deviation per degree of freedom (σ/ν) as a rescaled uncertainty in our observed radii, which better represents the error of these data. The bottom plot shows the best fitting model radius curve on top of the observed radial separations from the fit semimajor axis of the ring, $\Delta r = r - a$. We have listed the final fit parameters and chi-squared analysis in Table 1.

The best fitting pattern speed for this mode, 776.58208 ± 0.00169 /day, is strikingly close to the published mean motion of Cressida, the fourth moon from Uranus. Most recently, Showalter & Lissauer (2006) listed Cressida’s mean motion as 776.582789 ± 0.000059 /day. All three of the measurements of Cressida’s mean motion listed in Table 1 are well within the uncertainty of our detected pattern speed, supporting the proposed connection between this $m = 3$ structure of the η ring and Cressida.

To solidify that the $m = 3$ structure is real and is a result of perturbations from Cressida, we have inspected the alignment of the structure with Cressida. In this case, the η ring ($a = 47176.447$) is located exterior to the resonance ($a_{\text{res}} = 47171.51$), and the dynamical model predicts that one

Table 1
 η Ring $m = 3$ Best Fit

Parameter	Final Fit and Scaled Errors
a (km)	47176.447 ± 0.086
A_3 (km)	0.667 ± 0.113
δ_3 (°)	58.81 ± 6.12
Ω_p (°/day)	776.58208 ± 0.00169
n_{Cressida} (°/day)	$776.582789 \pm 0.000059^a$
n_{Cressida} (°/day)	$776.582414 \pm 0.000022^b$
n_{Cressida} (°/day)	$776.582447 \pm 0.000022^c$
χ^2	13.861
χ^2/ν	0.308
σ/ν (km)	0.555
N	49
# of parameters	4

Notes. Listed on top are the four fit parameters and their formal 1σ errors resulting from our final fit, where we have assumed an error of 0.555 km for each of the observed radii of the η ring. We also list three published mean motions of Cressida for comparison with our pattern speed. The chi-squared and reduced chi-squared below are from the initial fit assuming an error of 1 km for each radii. The unscaled errors of the parameters in the initial fit are roughly double the scaled errors from the final fit, in which we have used the standard deviation per degree of freedom as a universal error in the observed radii. The degrees of freedom $\nu = N - \#$ of fit parameters.

^a From Showalter & Lissauer (2006).

^b From Jacobson (1998).

^c From Pascu et al. (1998).

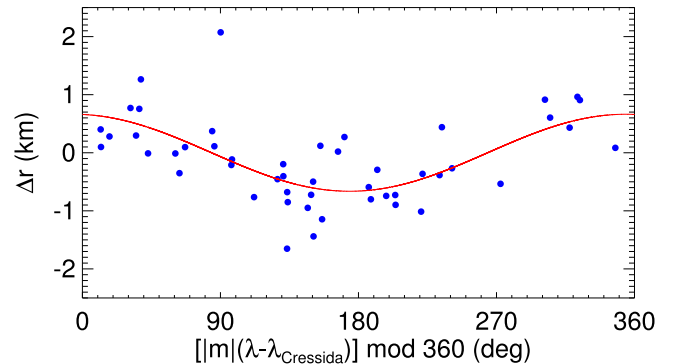


Figure 5. This plot shows the η ring structure in a reference frame tied to Cressida. One of the three outermost radial extents actually tracks Cressida, the others are located $\sim 120^\circ$ apart. We obtained longitudes of Cressida at various times using the ura091.bsp and ura112.bsp SPICE kernels, available at https://naif.jpl.nasa.gov/pub/naif/generic_kernels/spk/satellites/.

of the three outer radial extents should track the motion of Cressida. That is, as the $m = 3$ structure and Cressida both rotate around Uranus at $n_{\text{Cressida}} \simeq \Omega_p$, one of the apoapses is constantly aligned with Cressida. This can be confirmed by noting that the $m = 3$ structure has a phase offset $\delta_3 = 58.81 \pm 6.12$ (this is the longitude of one of the three periapsis), which is roughly 60° offset from Cressida’s longitude (359.50) at the epoch of the fit. We show this alignment more precisely in Figure 5, where we have determined the offset of each occultation scan longitude relative to Cressida’s longitude at the observation time, $|m|(\lambda - \lambda_{\text{Cressida}})$. The apoapse of the phase-wrapped structure lags the longitude of Cressida by only $6^\circ \pm 11^\circ$ (Cressida’s longitude is 0° and the fit sinusoid’s largest radial excursion

Table 2
Mass and Density of Cressida

A_3 (km)	Radius (km)	a (km)	a_{res} (km)	m_{Cressida} (kg)	ρ_{Cressida} (g cm $^{-3}$)
0.667 ± 0.113	41 ± 2	47176.447 ± 0.086	47171.51 ± 0.03	$(2.5 \pm 0.4) \times 10^{17}$	0.86 ± 0.16

Note. We list the variables needed to solve for the mass of Cressida using Equation (5). For the calculation of m_{Cressida} , we used $GM_{\text{Uranus}} = 5793951.3 \pm 4.4 \text{ km}^3 \text{ s}^{-2}$ from Jacobson (2014) and $G = (6.67408 \pm 31) \times 10^{-11} \text{ m}^3 \text{ kg}^{-1} \text{ s}^{-2}$ from <http://physics.nist.gov/cgi-bin/cuu/Value?bg>. Also note $\frac{2\alpha|f_d|}{j-1} \simeq 1.545$ when $j = m = 3$ for the case of the Cressida 3:2 ILR. The listed radius needed to calculate the density of Cressida comes from *Voyager 2* photometry (Karkoschka 2001a).

occurs at 354°). This suggests that the perturbations on the η ring are due to its proximity to the 3:2 ILR with Cressida.

Perhaps the most significant result of this work, shown in Table 2, is a determination of Cressida’s mass using Equation (5). Given $A_3 = 0.667 \pm 0.113 \text{ km}$ we find $m_{\text{Cressida}} = (2.5 \pm 0.4) \times 10^{17} \text{ kg}$. We use the effective radius for Cressida of $41 \pm 2 \text{ km}$ from Karkoschka (2001a) to calculate a density of $0.86 \pm 0.16 \text{ g cm}^{-3}$ for Cressida.

For our purposes, the η ring is outside the width of Cressida’s 3:2 ILR and the resulting estimation of A_m is reasonable, but we note that this is not necessarily the case for all of the other rings and resonances. Curious readers should note that to test the applicability of Equation (5), we have calculated a resonance half-width of $\sim 3.5 \text{ km}$ for Cressida’s 3:2 ILR using Equation (10.23) from Murray & Dermott (1999) along with our newly determined mass of Cressida. The other relevant variable inputs can be found in Tables 1 and 2. This half-width is less than the 5 km separation of the resonance and ring, confirming we are justified in using Equation (5). Note that the $\sim 1 \text{ km}$ resonance half-width quoted in the introduction was estimated by Porco & Goldreich (1987) and results from an approximation of the resonance half-width equation as well as a different satellite mass.

5. Discussion

Since the *Voyager 2* flyby of Uranus in 1986, several dynamicists have explored the stability of the inner Uranian moons. The moons Bianca, Cressida, Desdemona, Juliet, Portia, Rosalind, Cupid, Belinda, and Perdita are members of the most tightly packed system of moons in our solar system. Nicknamed the “Portia group” for their largest member, these satellites are thought to be unstable on short timescales compared to the age of the solar system. The stability of the Portia group is known to be highly sensitive to the masses of the individual satellites (French et al. 2015), which are not well constrained. In fact, the mass we provide for Cressida is the first direct measurement of an inner Uranian satellite’s mass. Past simulations (Duncan & Lissauer 1997; French & Showalter 2012; Quillen & French 2014; French et al. 2015) have relied on treating a range of possible masses for the inner Uranian satellites and suggest that Cressida may cross orbits with Desdemona in around 10^6 years (French & Showalter 2012), given our mass density. Incorporation of our mass for Cressida should further constrain the timescale of satellite orbit crossing (collisions) and allow a future work to determine the masses of some of the other satellites through their resonant interactions. Strictly speaking, our density measurement does not necessarily represent a common density of the inner moons. However, a lower average satellite density will generally result in collisions occurring in the more distant future.

Karkoschka (2001b) and Dumas et al. (2003) detected a possible water ice absorption feature in *Hubble Space*

Telescope near-infrared photometry of the largest inner moon, Puck. Combining this with the previously mentioned size estimates has formed the presumption that Cressida and the other inner Uranian moons are likely composed of mostly water ice with at least a veneer or contamination of dark material to explain their low albedo and flat gray spectra. The range in densities of the larger Uranian moons, determined from mass (Jacobson et al. 1992) and radius (Thomas 1988) measurements, have provided a presumed upper limit on the densities of the inner moons, usually with reference to the least dense major moon Miranda ($1.214 \pm 0.109 \text{ g cm}^{-3}$).³ In Figure 6, we plot our average density of Cressida versus radius along with other satellites in our solar system, after Hussmann et al. (2006). Cressida is about 50% denser than the inner icy moons of Saturn with comparable radii. It may be that Cressida, and the Uranian rings/moons in general, have either a lower porosity than these Saturnian analogs or they have higher amounts of non-icy contaminants, as inferred by Tiscareno et al. (2013). The contamination of denser and darker material may not be as high as previously expected, but it is substantial regardless.

This analysis shows that there is still information about Uranus’ rings and moons found in historical and ground-based data. Still, the best means of obtaining the Uranian moon masses and compositions, determining the ultimate fate of the Portia group, and understanding the intricate structure of the rings is, of course, a Uranus orbiter mission.

We would like to thank Phil Nicholson for his insights regarding ring occultation observations and both Phil Nicholson and Pierre-Yves Longaretti for several fruitful discussions concerning the forced radial amplitudes of ring particles orbiting near Lindblad resonances. We would also like to thank our anonymous reviewer for helpful suggestions and comments, ultimately improving the clarity of this work. This work was supported by the NASA Solar System Workings program grant NNX15AH45G.

Appendix

Included in Table 3 are the occultation observation data we used in this analysis of the η ring. The precise numbers for the ring’s position are derived from an analysis of the entire Uranian ring data set, including re-determined pole position (Pole R.A. = $77^\circ 31' 05.814$ and decl. = $15^\circ 16' 97.826$), standard gravitational parameter ($GM = 5.793956433 \times 10^6 \text{ km}^3 \text{ s}^{-2}$), gravitational harmonics ($J_2 = 3.340656 \times 10^{-3}$ and $J_4 = -3.148536 \times 10^{-5}$), and time offsets. The numbers therefore can deviate slightly from previously published values. We list each observation ID, observing location, ring plane intercept

³ https://ssd.jpl.nasa.gov/?sat_phys_par

Table 3
 η Ring Occultation Observation Geometry

ID	Observing Location	Star Name Catalog ID	$t_{\text{ring intercept}}$ (UTC)	r (km)	$r - r_{\text{fit}}$ (km)	$\lambda(^{\circ})$	Reference
1	Kuiper Airborne Obs.	U0 <i>Hipparcos</i> 71567	1977 Mar 10 17:48:26.95	47177.352	0.346	36.68	Elliot et al. (1977)
2	Kuiper Airborne Observatory	U0 <i>Hipparcos</i> 71567	1977 Mar 10 19:20:03.28	47176.465	0.673	153.51	Elliot et al. (1977)
3	Cerro Las Campanas Obs.	U5 UCAC2 25775788	1978 Apr 10 03:00:16.19	47178.519	2.107	46.24	Nicholson et al. (1978)
4	Cerro Las Campanas Obs.	U5 UCAC2 25775788	1978 Apr 10 03:50:16.64	47177.359	0.535	143.71	Nicholson et al. (1978)
5	Cerro Tololo Interamerican Obs.	U12 UCAC2 25096598	1980 Aug 15 22:20:37.70	47176.235	-0.087	22.05	Elliot et al. (1981a)
6	European Southern Obs. 1 m	U12 UCAC2 25096598	1980 Aug 15 19:24:18.97	47175.681	-0.476	171.95	Elliot et al. (1981a)
7	European Southern Obs. 1 m	U12 UCAC2 25096598	1980 Aug 15 22:20:36.26	47176.330	0.013	22.18	Elliot et al. (1981a)
8	Anglo-Australian Telescope	U13 <i>Hipparcos</i> 77434	1981 Apr 26 16:45:45.26	47176.726	-0.341	26.90	French et al. (1982)
9	Anglo-Australian Telescope	U13 <i>Hipparcos</i> 77434	1981 Apr 26 17:53:41.63	47176.877	-0.092	163.55	French et al. (1982)
10	European Southern Obs. 2 m	U14 <i>Hipparcos</i> 79085	1982 Apr 22 00:27:11.11	47175.767	-0.184	164.12	French et al. (1986a)
11	Cerro Las Campanas Obs.	U14 <i>Hipparcos</i> 79085	1982 Apr 21 23:07:45.20	47175.548	-0.314	24.83	French et al. (1986a)
12	Cerro Las Campanas Obs.	U14 <i>Hipparcos</i> 79085	1982 Apr 22 00:27:11.32	47174.793	-1.158	164.09	French et al. (1986a)
13	Tenerife	U14 <i>Hipparcos</i> 79085	1982 Apr 21 23:09:03.74	47176.060	-0.027	35.09	French et al. (1986a)
14	Cerro Tololo Interamerican Obs.	U14 <i>Hipparcos</i> 79085	1982 Apr 21 23:07:38.90	47175.718	-0.143	24.70	French et al. (1986a)
15	Cerro Tololo Interamerican Obs.	U14 <i>Hipparcos</i> 79085	1982 Apr 22 00:27:09.91	47175.595	-0.353	164.23	French et al. (1986a)
16	Mt. Stromlo	U15 UCAC2 23648038	1982 May 01 13:53:02.53	47176.249	0.275	27.01	French et al. (1986a)
17	Mt. Stromlo	U15 UCAC2 23648038	1982 May 01 15:01:45.77	47176.542	-0.119	162.76	French et al. (1986a)
18	Mt. Palomar	U16 UCAC2 23892052	1982 Jun 04 02:50:34.77	47175.991	-0.012	32.37	French et al. (1986a)
19	Mt. Palomar	U16 UCAC2 23892052	1982 Jun 04 03:50:47.86	47176.435	-0.464	156.73	French et al. (1986a)
20	South African Astronomical Obs.	U17 <i>Hipparcos</i> 80841	1983 Mar 24 22:05:13.10	47176.847	-0.238	35.29	French et al. (1986a)
21	Cerro Tololo Interamerican Obs.	U23 UCAC2 22735323	1985 May 04 02:28:59.92	47176.178	-0.003	318.94	French et al. (1988)
22	Cerro Tololo Interamerican Obs.	U23 UCAC2 22735323	1985 May 04 03:30:35.20	47176.885	0.774	229.93	French et al. (1988)
23	McDonald Obs.	U23 UCAC2 22735323	1985 May 04 03:37:42.72	47175.702	-0.133	221.66	French et al. (1988)
24	Cerro Tololo Interamerican Obs.	U25 UCAC2 22734194	1985 May 24 05:23:43.95	47176.565	0.747	316.13	French et al. (1988)
25	Cerro Tololo Interamerican Obs.	U25 UCAC2 22734194	1985 May 24 06:10:43.14	47176.151	0.340	233.85	French et al. (1988)
26	McDonald Obs.	U25 UCAC2 22734194	1985 May 24 05:22:06.85	47175.644	-0.154	326.24	French et al. (1988)
27	McDonald Obs.	U25 UCAC2 22734194	1985 May 24 06:17:47.01	47175.721	-0.124	223.28	French et al. (1988)
28	Mt. Palomar	U25 UCAC2 22734194	1985 May 24 05:23:00.51	47175.853	0.059	326.26	French et al. (1988)
29	Mt. Palomar	U25 UCAC2 22734194	1985 May 24 06:18:47.48	47175.497	-0.360	223.09	French et al. (1988)
30	IRTF	U28 UCAC2 22517254	1986 Apr 26 10:58:06.57	47176.433	-0.282	333.24	Tyler et al. (1986)
31	IRTF	U28 UCAC2 22517254	1986 Apr 26 12:34:39.87	47175.910	-0.632	215.97	Tyler et al. (1986)
32	IRTF	U1052 UCAC2 22296665	1988 May 12 10:56:55.69	47175.431	-0.563	293.09	Lane et al. (1986)
33	IRTF	U1052 UCAC2 22296665	1988 May 12 11:26:09.19	47176.094	-0.584	256.32	French et al. (1988)
34	IRTF	U83 UCAC2 22564036	1991 Jun 25 10:10:59.40	47176.545	-0.530	326.15	French et al. (1988)
35	IRTF	U83 UCAC2 22564036	1991 Jun 25 10:59:59.96	47176.530	-0.581	224.37	Unpublished
36	IRTF	U84 UCAC2 22563790	1991 Jun 28 07:47:36.36	47176.741	-0.197	306.15	Unpublished
37	IRTF	U84 UCAC2 22563790	1991 Jun 28 08:19:53.10	47175.300	-0.507	243.98	Unpublished
38	Cerro Tololo Interamerican Obs.	U9539 UCAC2 23016546	1993 Jun 30 04:57:33.67	47176.082	0.063	351.62	Unpublished
39	Cerro Tololo Interamerican Obs.	U9539 UCAC2 23016546	1993 Jun 30 05:54:55.13	47177.216	0.256	199.09	Unpublished
40	South African Astronomical Obs.	U134 UCAC2 23509999	1995 Sep 09 15:29:49.47	47175.948	0.126	31.36	Unpublished
41	South African Astronomical Obs.	U134 UCAC2 23509999	1995 Sep 09 16:57:52.04	47177.201	0.292	161.04	Unpublished
42	IRTF	U137 UCAC3 141-413386	1996 Mar 16 11:59:43.68	47176.716	0.936	178.95	Unpublished
43	IRTF	U137 UCAC3 141-413386	1996 Mar 16 12:43:23.55	47177.408	0.372	13.13	Unpublished
44	Mt. Palomar	U138 UCAC2 24243463	1996 Apr 10 09:27:44.07	47177.050	0.139	356.19	Unpublished
45	Mt. Palomar	U0201 UCAC2 27214859	2002 Jul 29 07:20:09.62	47177.709	0.829	74.55	Unpublished
46	Mt. Palomar	U0201 UCAC2 27214859	2002 Jul 29 07:29:17.80	47175.005	-0.807	117.00	Unpublished
47	<i>Voyager 2</i> —RSS		1986 Jan 24 19:50:59.23	47176.817	0.080	343.08	French et al. (1991)
48	<i>Voyager 2</i> —RSS		1986 Jan 24 22:44:28.11	47176.557	0.375	197.13	French et al. (1991)
49	<i>Voyager 2</i> —PPS	β Per <i>Hipparcos</i> 14576	1986 Jan 24 19:36:54.98	47176.041	0.132	110.96	French et al. (1991)

Note. The precise numbers for the ring's position are derived from an analysis of the entire Uranian ring data set, including re-determined pole position, GM , J_2 , J_4 , and time offsets. We used an epoch time, t_0 , of UTC 1977 March 10 20:00:00.00 for all fits of this data set. The times, t , listed in this table refer to the exact time of the ray intercept in the ring plane for each occultation observation. The ring radii and longitudes are those observed at these times, where longitudes are measured in the prograde direction from the ascending node of Uranus' equator on the Earth's equator of the J2000 epoch. The residuals show separation of each observations' radii and the $m = 3$ model radii.

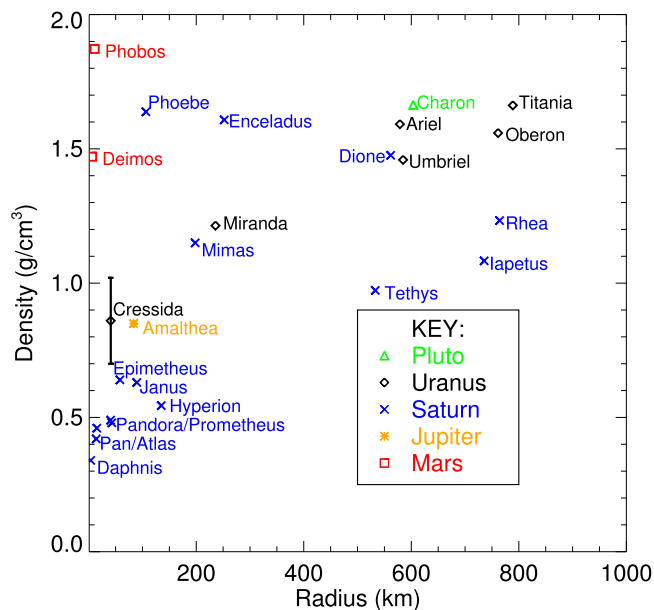


Figure 6. The known densities of selected satellites in the solar system are plotted vs. their radii. We represent the individual moons associated with particular planets using the point styles and colors labeled in the lower right of the plot.

time of the relevant electromagnetic wave observed, detected mid-radius of the η ring, $m = 3$ fit residuals, longitude of the observation, longitude of Cressida at this time, and reference to publications including the observation. Longitudes are measured in the prograde direction from the ascending node of Uranus' equator on the Earth's equator of the J2000 epoch. French et al. (1988) have included all observations from 1977 to 1986 in their most recent fit, but more recent observations are unpublished.

ORCID iDs

Robert O. Chancia <https://orcid.org/0000-0002-7867-7674>

Matthew M. Hedman <https://orcid.org/0000-0002-8592-0812>

Richard G. French <https://orcid.org/0000-0002-9858-9532>

References

- Bhattacharyya, J. C., & Kuppaswamy, K. 1977, *Natur*, **267**, 331
 Colwell, J. E., Horn, L. J., Lane, A. L., et al. 1990, *Icar*, **83**, 102
 Dumas, C., Smith, B. A., & Terrile, R. J. 2003, *AJ*, **126**, 1080
 Duncan, M. J., & Lissauer, J. J. 1997, *Icar*, **125**, 1
 Elliot, J. L. 1979, *ARA&A*, **17**, 445
 Elliot, J. L., Dunham, E., & Mink, D. 1977, *Natur*, **267**, 328
 Elliot, J. L., Elias, J. H., French, R. G., et al. 1983, *Icar*, **56**, 202
 Elliot, J. L., French, R. G., Frogel, J. A., et al. 1981a, *AJ*, **86**, 444
 Elliot, J. L., French, R. G., Meech, K. J., & Elias, J. H. 1984, *AJ*, **89**, 1587
 Elliot, J. L., Frogel, J. A., Elias, J. H., et al. 1981b, *AJ*, **86**, 127
 Elliot, J. L., Glass, I. S., French, R. G., & Kangas, J. A. 1987, *Icar*, **71**, 91
 Elliot, J. L., & Nicholson, P. D. 1984, in *IAU Coll. 75: Planetary Rings*, ed. R. Greenberg & A. Brahic (Tucson, AZ: Univ. Arizona Press), **25**
 French, R. G., Dawson, R. I., & Showalter, M. R. 2015, *AJ*, **149**, 142
 French, R. G., Elliot, J. L., & Allen, D. A. 1982, *Natur*, **298**, 827
 French, R. G., Elliot, J. L., French, L. M., et al. 1988, *Icar*, **73**, 349
 French, R. G., Elliot, J. L., & Levine, S. E. 1986a, *Icar*, **67**, 134
 French, R. G., Kangas, J. A., & Elliot, J. L. 1986b, *Sci*, **231**, 480
 French, R. G., & Nicholson, P. D. 1995, *BAAS*, **27**, 857
 French, R. G., Nicholson, P. D., Hedman, M. M., et al. 2016a, *Icar*, **279**, 62
 French, R. G., Nicholson, P. D., McGhee-French, C. A., et al. 2016b, *Icar*, **274**, 131
 French, R. G., Nicholson, P. D., Porco, C. C., & Marouf, E. A. 1991, in *Uranus, Dynamics and structure of the Uranian Rings*, ed. J. T. Bergstrahl, E. D. Miner, & M. S. Matthews (Tucson, AZ: Univ. Arizona Press), **327**
 French, R. G., Roques, F., Nicholson, P. D., et al. 1996, *Icar*, **119**, 269
 French, R. S., & Showalter, M. R. 2012, *Icar*, **220**, 911
 Goldreich, P., & Porco, C. C. 1987, *AJ*, **93**, 730
 Goldreich, P., & Tremaine, S. 1982, *ARA&A*, **20**, 249
 Gresh, D. L., Marouf, E. A., Tyler, G. L., Rosen, P. A., & Simpson, R. A. 1989, *Icar*, **78**, 131
 Hedman, M. M., Nicholson, P. D., Baines, K. H., et al. 2010, *AJ*, **139**, 228
 Hussmann, H., Sohl, F., & Spohn, T. 2006, *Icar*, **185**, 258
 Jacobson, R. A. 1998, *AJ*, **115**, 1195
 Jacobson, R. A. 2014, *AJ*, **148**, 76
 Jacobson, R. A., Campbell, J. K., Taylor, A. H., & Synnott, S. P. 1992, *AJ*, **103**, 2068
 Karkoschka, E. 2001a, *Icar*, **151**, 69
 Karkoschka, E. 2001b, *Icar*, **151**, 51
 Klemola, A. R., & Marsden, B. G. 1977, *AJ*, **82**, 849
 Klemola, A. R., & Mink, D. J. 1991, *AJ*, **102**, 389
 Klemola, A. R., Mink, D. J., & Elliot, J. L. 1981, *AJ*, **86**, 138
 Kumar, K., de Pater, I., & Showalter, M. R. 2015, *Icar*, **254**, 102
 Lane, A. L., West, R. A., Nelson, R. M., et al. 1986, *Sci*, **233**, 65
 Lissauer, J. J. 1995, *Icar*, **114**, 217
 Markwardt, C. B. 2009, in *ASP Conf. Ser. 411, Astronomical Data Analysis Software and Systems XVIII*, ed. D. A. Bohlender, D. Durand, & P. Dowler (San Francisco, CA: ASP), **251**
 Millis, R. L., & Wasserman, L. H. 1978, *AJ*, **83**, 993
 Millis, R. L., Wasserman, L. H., & Birch, P. V. 1977, *Natur*, **267**, 330
 Mink, D. J., & Klemola, A. 1982, *AJ*, **87**, 1881
 Mink, D. J., & Klemola, A. 1985, *AJ*, **90**, 1894
 Murray, C. D., & Dermott, S. F. 1999, *Solar System Dynamics* (New York: Cambridge Univ. Press)
 Murray, C. D., & Thompson, R. P. 1988, *VA*, **32**, 225
 Murray, C. D., & Thompson, R. P. 1990, *Natur*, **348**, 499
 Nicholson, P. D., French, R. G., Hedman, M. M., Marouf, E. A., & Colwell, J. E. 2014a, *Icar*, **227**, 152
 Nicholson, P. D., French, R. G., McGhee-French, C. A., et al. 2014b, *Icar*, **241**, 373
 Nicholson, P. D., Matthews, K., & Goldreich, P. 1981, *AJ*, **86**, 596
 Nicholson, P. D., McLeod, B. A., Gilmore, G., Buie, M. W., & Matthews, K. 1988, *AJ*, **95**, 562
 Nicholson, P. D., Persson, S. E., Matthews, K., Goldreich, P., & Neugebauer, G. 1978, *AJ*, **83**, 1240
 Pasco, D., Rohde, J. R., Seidelmann, P. K., et al. 1998, *AJ*, **115**, 1190
 Porco, C. C., & Goldreich, P. 1987, *AJ*, **93**, 724
 Porco, C. C., & Nicholson, P. D. 1987, *Icar*, **72**, 437
 Quillen, A. C., & French, R. S. 2014, *MNRAS*, **445**, 3959
 Showalter, M. R. 2011, in *EPSC-DPS Joint Meeting 2011 The Rings of Uranus: Shepherd, or Not?*, **1224**
 Showalter, M. R., & Lissauer, J. J. 2003, in *IAU Circ., No. 8209*, ed. D. W. E. Green (Cambridge: Cambridge Univ. Press), **1**
 Showalter, M. R., & Lissauer, J. J. 2006, *Sci*, **311**, 973
 Sicardy, B., Combes, M., Brahic, A., et al. 1982, *Icar*, **52**, 454
 Smith, B. A., Soderblom, L. A., Beebe, R., et al. 1986, *Sci*, **233**, 43
 Taylor, G. E. 1973, *JBA*, **83**, 352
 Thomas, P., Weitz, C., & Veverka, J. 1989, *Icar*, **81**, 92
 Thomas, P. C. 1988, *Icar*, **73**, 427
 Tiscareno, M. S., Hedman, M. M., Burns, J. A., & Castillo-Rogez, J. 2013, *ApJL*, **765**, L28
 Tyler, G. L., Eshleman, V. R., Hinson, D. P., et al. 1986, *Sci*, **233**, 79